The Journal of Experimental Biology 214, 432-444
© 2011. Published by The Company of Biologists Ltd
doi:10.1242/jeb.046375

RESEARCH ARTICLE

Aerodynamic effects of corrugation in flapping insect wings in hovering flight

Xue Guang Meng*, Lei Xu and Mao Sun

Ministry-of-Education Key Laboratory of Fluid Mechanics, Beijing University of Aeronautics and Astronautics, Beijing, China

*Author for correspondence (mengxg.hi@163.com)

Accepted 7 October 2010

SUMMARY

We have examined the aerodynamic effects of corrugation in model insect wings that closely mimic the wing movements of hovering insects. Computational fluid dynamics were used with Reynolds numbers ranging from 35 to 3400, stroke amplitudes from 70 to 180 deg and mid-stroke angles of incidence from 15 to 60 deg. Various corrugated wing models were tested (care was taken to ensure that the corrugation introduced zero camber). The main results are as follows. At typical mid-stroke angles of incidence of hovering insects (35–50 deg), the time courses of the lift, drag, pitching moment and aerodynamic power coefficients of the corrugated wings are very close to those of the flat-plate wing, and compared with the flat-plate wing, the corrugation changes (decreases) the mean lift by less than 5% and has almost no effect on the mean drag, the location of the center of pressure and the aerodynamic power required. A possible reason for the small aerodynamic effects of wing corrugation is that the wing operates at a large angle of incidence and the flow is separated: the large angle of incidence dominates the corrugation in determining the flow around the wing, and for separated flow, the flow is much less sensitive to wing shape variation. The present results show that for hovering insects, using a flat-plate wing to model the corrugated wing is a good approximation.

Key words: insect, flapping wing, wing corrugation, aerodynamics.

INTRODUCTION

Flapping flight is employed by most flying insects, birds and bats. Scientists have long been interested in the aerodynamics of flapping wings, and recently, the aerodynamics of small insects is gaining more attention because of the possible applications in micro-aerial vehicles (MAVs). Much work has been done on the aerodynamics of flapping insect wings using experimental and computational methods (e.g. Ellington et al., 1996; Dickinson et al., 1999; Usherwood and Ellington, 2002a; Usherwood and Ellington, 2002b; Sane and Dickinson, 2001; Liu et al., 1998; Sun and Tang, 2002; Wang et al., 2004), and considerable understanding of the aerodynamic-force-generation mechanisms has been achieved. In these studies, flat-plate model wings were employed; however, it is well known that insect wings are corrugated (e.g. Dudley, 2000). The authors of the studies using flat-plate wings have implicitly assumed that the corrugation has a minor effect on aerodynamic forces of the wings. It is of great interest to test this assumption, and to know whether the wing corrugation significantly influences the aerodynamic force production of flying insects.

There has been some work on the effects of wing corrugation under steady flow conditions (e.g. Rees, 1975a; Kesel, 2000; Vargas et al., 2008). Rees tested a corrugated wing (model hoverfly wing) and a smooth wing [the section of the smooth wing was formed by drawing a smooth 'envelope' through the corner points of the corrugated section (Rees, 1975a)]. Lift and drag were measured at Reynolds numbers (*Re*) of 450, 800 and 900. He found little difference in aerodynamic forces between the smooth and corrugated models. His flow visualization experiment showed that flow over the corrugated wing seemed to introduce some fluid becoming trapped in the folds, where it was either stagnant or recirculating, and the main flow seemed to behave as if the folds were solidly infilled. Kesel tested various corrugated sectional profiles at *Re*=7880 and 10^4 (Kesel, 2000). The profiles were constructed using measurements taken from the cross sections at different locations of a dragonfly forewing. His results showed that the corrugated profile had a slightly better aerodynamic performance than the corresponding flat-plate airfoils. Recently, Vargas et al. conducted a comprehensive computational study of a corrugated airfoil in the flow velocity range of gliding dragonflies and in that of fixed-wing micro-aerial vehicles (Vargas et al., 2008). They also computed the flows of the corresponding profiled airfoil (the smoothed counterpart) and flat-plate airfoil. Their results demonstrated that the corrugated wing performed as well as, and at times slightly better than, the profiled airfoil and the flat-plate airfoil.

These studies (Rees, 1975a; Kesel, 2000; Vargas et al., 2008) were conducted for fixed-wing flight (gliding), and the flow was steady. Luo and Sun conducted a computational study on a corrugated wing operating under unsteady flow condition, but it was only for a sweeping motion (the wing started from still air and rotated for approximately 150 deg) (Luo and Sun, 2005). To our knowledge, the effects of wing corrugation on aerodynamic forces of wings in flapping motion have not been reported. It is important to know whether the effects are significant, or the effects are negligible, and smooth model wings can be used in experimental and computational studies. Another problem with the previous studies (Rees, 1975a; Kesel, 2000; Vargas et al., 2008) was that it was not clear whether or not the corrugated wing and the smoothed counterpart had the same camber. As a result, it is uncertain whether the slightly better aerodynamic performance is due to the camber effect or the corrugation effect.

In the present study, we address the above questions by studying the aerodynamic effects of corrugation of wings in flapping motion using the method of computational fluid dynamics (CFD). Different corrugation patterns are considered. The effects of wing corrugation

were investigated by comparing the aerodynamic forces and flows between corrugated and flat-plate wings. Care was taken to ensure that the corrugated wing introduced zero camber. Our group has studied the effect of wing camber recently (Du and Sun, 2010). Here, we try to isolate the effect of wing corrugation. It is possible that there exists camber–corrugation interaction, and this will be studied in our future work. Wing kinematics in forward flight is generally very different from that in hovering flight (e.g. in forward flight, the stroke plane tilts forward, the angles of incidence of the wings are lower and the down- and upstrokes are asymmetrical), and hence the corrugation effect might be different for these two types of flight. Because in each type of flight, there are many factors to consider (Reynolds number, stroke amplitude, angle of incidence, wing aspect ratio, corrugation pattern, etc.), it is better to restrict the present study to one type of flight. As a first step, we have studied the corrugation effects in hovering flight.

MATERIALS AND METHODS

The corrugated model wings and the flat-plate wing

To study the effects of wing corrugation, we used four model wings: three corrugated wings with different corrugation patterns and one flat-plate wing. A rectangular planform wing with a length (R) to chord length (c) ratio of 3 (aspect ratio of 6) was used for the model wings. The wing sections of these model wings are shown in Fig. 1. The thickness of the flat-plate wing was 0.03c. The other wings were the same thickness, but their chordal profiles were corrugated. On the basis of the study by Rees (Rees, 1975b) on the sectional shapes of wings of some insects (two dipterans and a hymenopteran), it is reasonable to model the corrugation as triangular waves; between the leading edge and a point 0.5–0.7c from the leading edge. For model A, the corrugations were of six waves between the leading edge and a point 0.6c from the leading edge (Fig. 1). For model B, six waves were also used but they were between 0.1c and 0.7c from the leading edge (Fig. 1). For model C, four waves were used between 0.1c and 0.5c from the leading edge (Fig. 1). In studying the structural properties of insect wings, Rees also modeled the corrugations as triangular waves (Rees, 1975a; Rees, 1975b). He measured the wavelengths and amplitudes of the corrugations of seven species of insect (see table 1 in Rees, 1975b), and the average values of the wavelength and the amplitude of the corrugations were approximately 0.1c and 0.03c, respectively. In the present study, we set the wavelength of the triangular wave as 0.1c and the amplitude as 0.05c. The corrugation amplitude used here (0.05c) is larger than the measured value (average, 0.03c). The reason for this is that the present work tested the assumption that the corrugation does not significantly influence the aerodynamic force production and so it is safe to use a value that is a little larger than the average value.

The wing motion

The flapping motion is outlined in Fig. 2. O,X,Y,Z is an inertial system (fixed on the body of an insect in hovering or constant-speed flight) and o,x,y,z is a non-inertial coordinate system fixed on the flapping wing. The flapping motion of the wing is approximated as follows. The motion consists of two parts: the translation (azimuthal rotation, about the Z-axis; see Fig. 2A) and the rotation (flip rotation, about the y-axis; see Fig. 2A); the out-of-plane motion of the wing (deviation) is ignored. The time variation of the translation speed ($\dot{\phi}$) of the wing is approximated by the simple harmonic function:

$$\dot{\phi} = -\pi n \Phi \sin(2\pi n t), \quad (1)$$

where ‘˙’ represents differentiation with respect to time t, ϕ is the positional angle, n the wingbeat frequency and Φ the stroke amplitude. The angle of incidence of the wing (α) takes a constant value during the downstroke or upstroke translation (the constant value is denoted by α_d for the downstroke translation and α_u for the upstroke translation; α_d and α_u are known as mid-stroke angles of incidence); around stroke reversal, the wing flips and α changes with time, also according to the simple harmonic function. The function representing the time variation of α during the supination at the mth cycle is:

$$\alpha = \alpha_d + a\{(t - t_1) - \frac{\Delta t_r}{2\pi}\sin[2\pi(t - t_1)/\Delta t_r]\},\ t_1 \le t \le t_1 + \Delta t_r\ , \quad (2a)$$

where Δt_r is the time interval of wing rotation during the stroke reversal and a is a constant:

$$a = (180\,\text{deg} - \alpha_u - \alpha_d)/\Delta t_r, \quad (2b)$$

and t_1 is the time when the wing rotation starts:

$$t_1 = mT - 0.5T - \Delta t_r/2. \quad (2c)$$

Pronation can be expressed in the same way. It is assumed that the axis of the pitching rotation is located at 0.25c from the leading edge of the wing. For many insects, Eqns 1 and 2 are good approximations to the measured data (Liu and Sun, 2008; Ellington, 1984). From Eqns 1 and 2, we see that to prescribe the flapping motion, Φ, the wingbeat frequency (n), Δt_r and the angles of incidence in the downstroke and upstroke translations, α_d and α_u, respectively, need to be given.

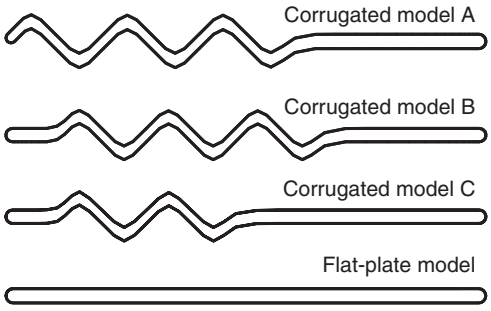

Fig. 1. Sections of the model wings.

The flow equations and the solution method

The governing equations of the flow are the three-dimensional (3-D) incompressible unsteady Navier–Stokes equations. They have the following dimensionless form:

$$\nabla \cdot \mathbf{u} = 0 \quad (3)$$

$$\frac{\partial \mathbf{u}}{\partial t} + \mathbf{u}\cdot\nabla\mathbf{u} = -\nabla p + \frac{1}{Re}\nabla^2\mathbf{u}\ , \quad (4)$$

where $\mathbf{u}$ is the non-dimensional fluid velocity field, p is the non-dimensional fluid pressure, ∇ is the gradient operator and ∇^2 is the Laplacian operator. In the non-dimensionalization, U, c and c/U are taken as reference velocity, length and time, respectively (U is the mean flapping velocity, defined as U=2$\Phi n r_2$ where r_2 is the radius of second moment of wing area); Re is defined as Re=cU/ν, where ν is the kinematic viscosity of the air. Similar to our previous work (e.g. Sun and Tang, 2002; Sun and Yu, 2006), Eqns 3 and 4 are solved using an algorithm based on the method of artificial compressibility. The algorithm was developed by Rogers and Kwak (Rogers and Kwak, 1990) and Rogers et al. (Rogers et al., 1991) and is outlined below.

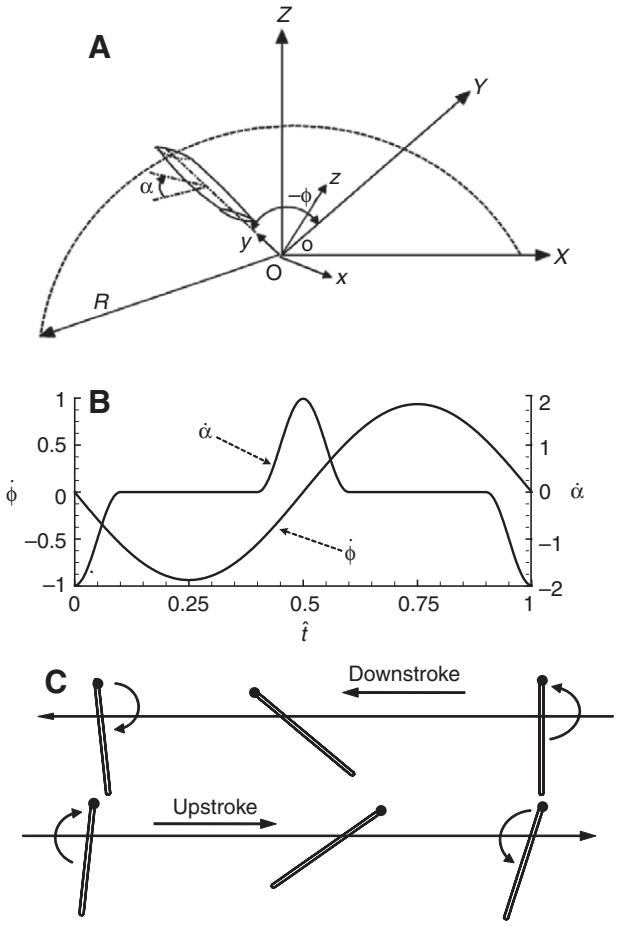

Fig. 2. (A) Sketches of the reference frames and wing motion. O,X,Y,Z is an inertial frame, with the X–Y plane horizontal and coincident with the stroke plane. o,x,y,z is a frame fixed on the wing, with the x-axis along the wing chord and the y-axis along the wing span. (B) Time courses of the translation speed ($\dot{\phi}$) and the rotational speed ($\dot{\alpha}$) in one cycle. ϕ, positional angle of the wing; α, angle of incidence of the wing; R, wing length. (C) A sketch of the motion of a section of the wing; a dot is placed on the leading edge of the wing section; $\hat{t}$, non-dimensional time.

The equations are first transformed from the Cartesian coordinate system (X,Y,Z,τ) to the curvilinear coordinate system (ξ,η,ζ,τ) using a general time-dependent coordinate transformation. For a flapping wing in the present study, a body-fixed coordinate system (o,x,y,z) is also employed (Fig. 2). The inertial coordinates (O,X,Y,Z) are related to the body-fixed coordinates (o,x,y,z) through a known relationship, and the transformation metrics in the inertial coordinate system $(\xi_x,\xi_y,\xi_z,\xi_\tau)$, $(\eta_x,\eta_y,\eta_z,\eta_\tau)$ and $(\zeta_x,\zeta_y,\zeta_z,\zeta_\tau)$, which are needed in the transformed Navier–Stokes equations, can be calculated from those in the body-fixed, non-inertial coordinate system (ξ_x,ξ_y,ξ_z), (η_x,η_y,η_z) and $(\zeta_x,\zeta_y,\zeta_z)$, which need to be calculated only once. The time derivatives of the momentum equations are differenced using a second-order, three-point backward difference formula. To solve the time-discretized momentum equations for a divergence free velocity at a new time level, a pseudo-time level is introduced into the equations and a pseudo-time derivative of pressure, divided by an artificial compressibility constant, is introduced into the continuity equation. The resulting system of equations are iterated in pseudo-time until the pseudo-time derivative of pressure approaches zero, thus, the divergence of the velocity at the new time level approaches zero. The derivatives of the viscous fluxes in the momentum equation are approximated using second-order central differences. For the derivatives of convective fluxes, upwind differencing based on the flux-difference splitting technique is used. A third-order upwind differencing is used at the interior points and a second-order upwind differencing is used at points next to boundaries. Details of this algorithm can be found in papers by Rogers and Kwak (Rogers and Kwak, 1990) and Rogers et al. (Rogers et al., 1991).

The computational grids are generated using a Poisson solver, which is based on the work of Hilgenstock (Hilgenstock, 1988). They are O–H-type grids. The grids will be further described in the Results, and discussion and examination of the convergence of solutions will also be conducted there. Boundary conditions are as follows. For far-field boundary conditions, at inflow boundary, the velocity components are specified as free-stream conditions (determined by flight speed), whereas pressure is extrapolated from the interior; at the outflow boundary, pressure is set equal to the free-stream static pressure and the velocity is extrapolated from the interior. On the wing surface, impermeable wall and non-slip conditions are applied and the pressure is obtained through the normal component of the momentum equation written in the moving grid system.

Once the Navier–Stokes equations are numerically solved, the fluid velocity components and pressure at discretized grid points for each time step are available. The aerodynamic forces and moment [lift, L, drag, D and pitching moment, M (moment about the spanwise axis at quarter chord)] acting on the wing are calculated from the

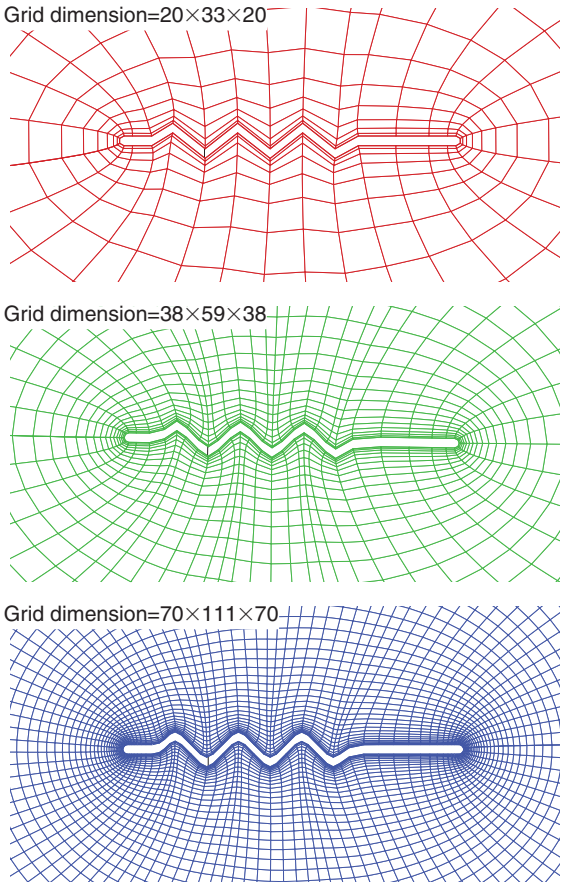

Fig. 3. Portions of the grids of corrugated model wing B.

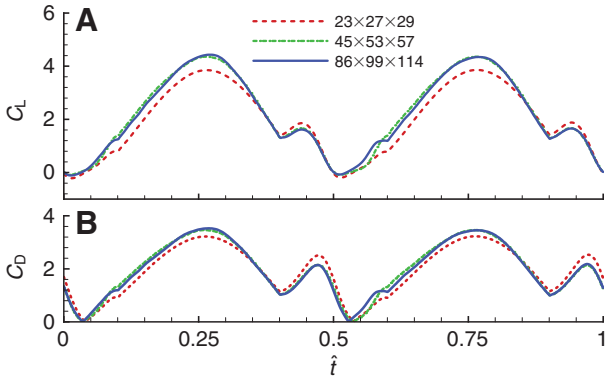

Fig. 4. Time courses of the lift (C_L) and drag (C_D) coefficients of the flat-plate wing for different grids. $\hat{t}$, non-dimensional time.

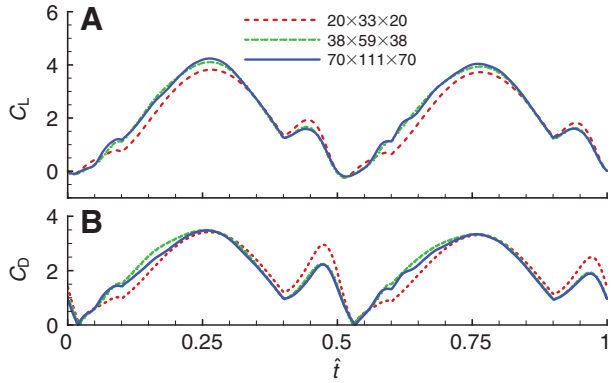

Fig. 5. Time courses of the lift (C_L) and drag (C_D) coefficients of corrugated model wing B for different grids. $\hat{t}$, non-dimensional time.

pressure and the viscous stress on the wing surface. The lift, drag and moment coefficients (denoted as C_L, C_D and C_M, respectively) are defined as follows: $C_L=L/0.5\rho U^2S$, $C_D=D/0.5\rho U^2S$ and $C_M=M/0.5\rho U^2Sc$, where ρ is the fluid density and S is the wing area.

Non-dimensional parameters that affect the aerodynamic force coefficients

For a wing of given geometry, solution of the non-dimensional Navier–Stokes equations (Eqns 3 and 4) under given boundary conditions gives C_L, C_D and C_M.

The only non-dimensional parameter in the Navier–Stokes equations is Re. The boundary condition of the Navier–Stokes equations is determined by the wing motion. It can be shown that after non-dimensionalizing Eqns 1 and 2, non-dimensional parameters that prescribe the flapping motion of the wing are Φ, Δt_r^* (non-dimensional time interval of wing rotation, non-dimensionalized by c/U), α_d and α_u. Therefore, non-dimensional parameters that might affect C_L, C_D and C_M are Re, Φ, Δt_r^*, α_d and α_u.

As observed in Ellington's comprehensive experiments on wing kinematics of many hovering insects (Ellington, 1984), Δt_r^* does not change greatly between insects (Δt_r^* is approximately 20% of the wingbeat cycle). Furthermore, Wu and Sun have shown that C_L and C_D and are only slightly affected by change in Δt_r^* (Wu and Sun, 2004). Thus in the present study we fixed Δt_r^* as 20% of the wingbeat cycle and only changed Re, Φ and α.

RESULTS AND DISCUSSION

Code validation and grid resolution test

The code used in this study is the same as that in Sun and Tang (Sun and Tang, 2002). It was tested by measured unsteady aerodynamic forces on a flapping model fruit fly wing (Sun and Wu, 2003), on revolving model wings (Wu and Sun, 2004) and on a pair of wing in 'fling motion' (Sun and Yu, 2006). These tests showed that the unsteady aerodynamic forces computed by the present CFD code agreed well with the experimental measurements.

Previous work by our group (Luo and Sun, 2005) showed that a grid with approximately 110 points around the wing section could resolve the flow around the corrugated wing. In the present study, grids with dimensions of approximately 70×110×70 in the normal direction, around the wing section and in the spanwise direction, respectively, were used for the corrugated wings (for model wing A: 65×105×70; for model wing B: 70×111×70; for model wing C: 65×113×70). A grid with dimensions 86×99×114, in the normal direction, around the wing section and in the spanwise direction, respectively, was used for the flat-plate wing. The first layer grid thickness was 0.001c. In the normal direction, the outer boundary was set at 20c from the wing and in the spanwise direction the boundary was set at 6c from the wing. The non-dimensional time step (non-dimensionalized by c/U) was 0.02 (the effect of the time step value was studied and it was found that a numerical solution effectively independent of the time step was achieved if the time step value was ≤0.02).

In order to give some quantitative assessment of the accuracy of the solution, we tested the following grids. For the corrugated wing (model wing B), two more grids, 38×59×38 (first layer grid thickness was 0.002) and 20×33×20 (first layer grid thickness was 0.004), were considered. Two more grids were also considered for the flat-plate wing, 45×53×57 (first layer grid thickness was 0.002) and 23×27×29 (first layer grid thickness was 0.004). As an example, the three grids for the corrugated wing (course: 20×33×20; medium: 38×59×38; dense: 70×111×70) are shown in Fig. 3 (note that in each refinement, the grid dimension in each

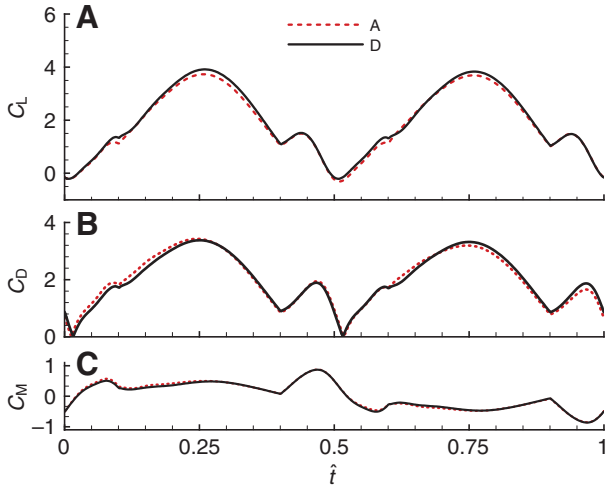

Fig. 6. Time courses of the lift (C_L), drag (C_D) and pitching moment (C_M) coefficients of corrugated model wing A and the flat-plate wing at Re=200, Φ=150 deg and α_d (α_u)=40 deg. The lines A and D indicate corrugated model wing A and the flat-plate wing, respectively. Re, Reynolds number; Φ, stroke amplitude; α_d and α_u, down- and upstroke angles of incidence, respectively. $\hat{t}$, non-dimensional time.

direction is approximately doubled). Calculations were performed using the above grids for the case of α_d (and α_u)=40 deg and *Re*=3400 (this *Re* was the highest considered in this study).

For a clear description of the results, we express the time during a cycle as a non-dimensional parameter, $\hat{t}$, such that $\hat{t}$=0 at the start of a downstroke, and $\hat{t}$=1 at the end of the subsequent upstroke. The computed results of the flat-plate wing and the corrugated wing are shown in Figs 4 and 5, respectively. It can be seen that for both the flat-plate wing and the corrugated wing, the first grid refinement produces a relatively large change in the results, but the second grid refinement produces a very small change in the results.

For the corrugated wing, using the first grid refinement (from grid 20×33×20 to grid 38×59×38), the mean magnitudes of change in C_L and C_D are 0.24 and 0.29, respectively, and the numbers for the second grid refinement (from grid 38×59×38 to grid 70×111×70) are 0.06 and 0.08, respectively. The ratio between the changes in C_L (0.06/0.24) and that in C_D (0.08/0.29) are approximately 1/4, as expected for the second-order method. Let us use the above data to give an estimate of the accuracy of the solution obtained by grid 70×111×70. Suppose that the grid is further refined (doubling the grid dimension in each direction), one could expect that the changes in C_L and C_D would be approximately 0.015 and 0.02, respectively (0.06/4=0.015 and 0.08/4=0.02). Based on the 1/4-convergence ratio, we could estimate that the solution by grid 70×111×70 has errors in C_L and C_D of 0.02 and 0.027, respectively [0.015×(4/3)=0.02 and 0.02×(4/3)=0.027]. The mean C_L and C_D are 2.09 and 1.98, respectively. Therefore, it is estimated that the solution based on the grid 70×111×70 has a ~1% error in the mean C_L and C_D.

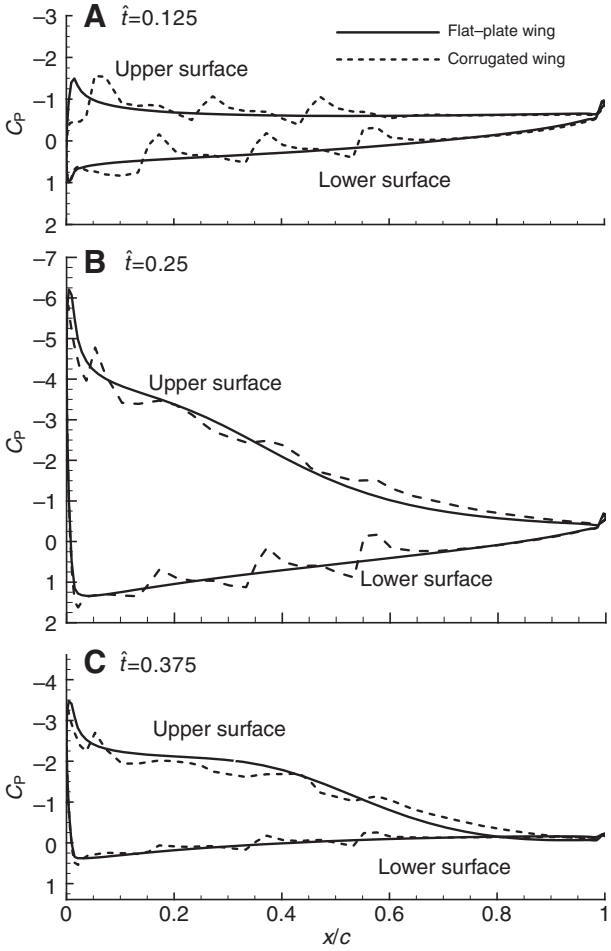

Fig. 7. Surface pressure distributions (C_p) at half-wing length of corrugated model wing A and the flat-plate wing at various times during a downstroke at *Re*=200, Φ=150 deg, α_d (and α_u)=40 deg. *Re*, Reynolds number; Φ, stroke amplitude; α_d and α_u, down- and upstroke angles of incidence, respectively; $\hat{t}$, non-dimensional time; *c*, chord length.

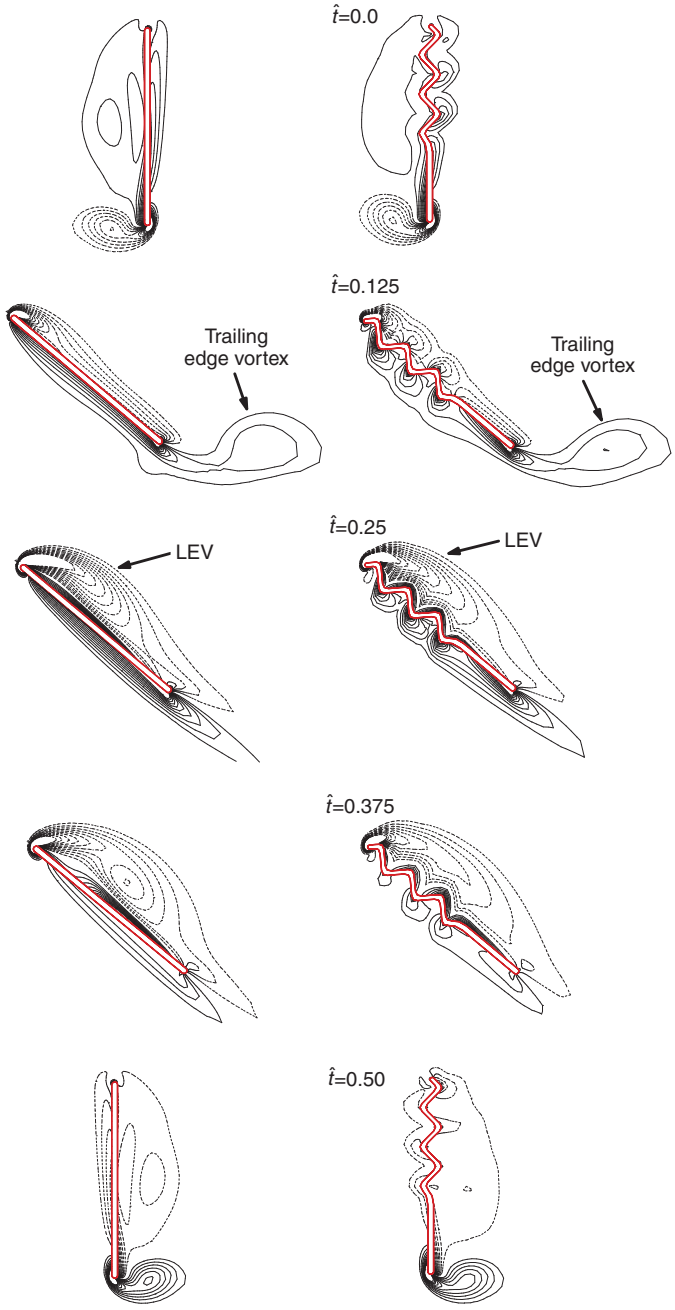

Fig. 8. Vorticity plots at half-wing length of the flat-plate wing and corrugated model wing A at various times during a downstroke at *Re*=200, Φ=150 deg, α_d (and α_u)=40 deg. *Re*, Reynolds number; Φ, stroke amplitude; α_d and α_u, down- and upstroke angles of incidence, respectively. Solid and broken lines indicate positive and negative vorticity, respectively. The magnitude of the non-dimensional vorticity at the outer contour is 4 and the contour interval is 3. $\hat{t}$, non-dimensional time; LEV, leading edge vortex.

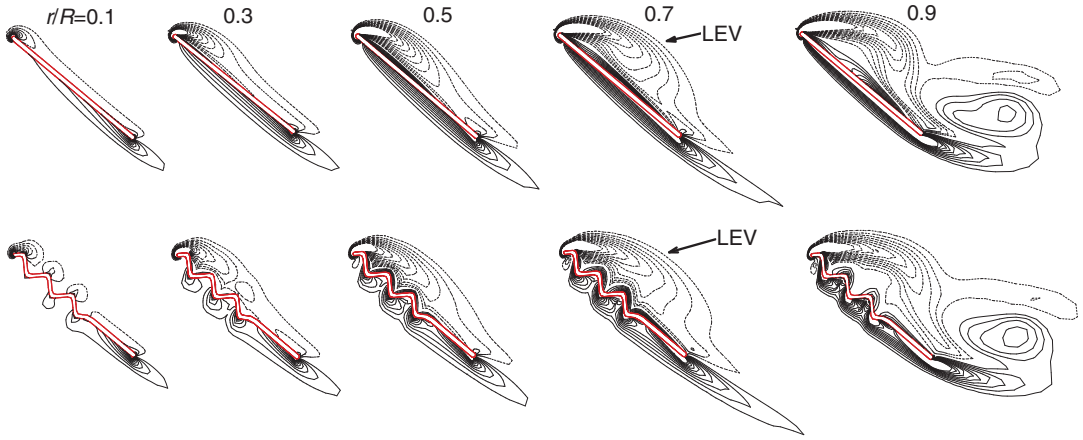

Fig. 9. Vorticity plots at various spanwise locations of the flat-plate wing and corrugated model wing A at the middle downstroke ($\hat{t}$=0.25) at *Re*=200, Φ=150 deg, α_d (and α_u)=40 deg. *Re*, Reynolds number; Φ, stroke amplitude; α_d and α_u, down- and upstroke angles of incidence, respectively. $\hat{t}$, non-dimensional time; *r*, radial distance along the wing length; *R*, wing length; LEV, leading edge vortex.

For the flat-plate wing, using the first grid refinement, the mean magnitudes of changes in C_L and C_D are 0.31 and 0.23, respectively, and using the second refinement, the values are 0.07 and 0.07. Again, the ratio between the changes in C_L (0.07/0.31) and that in C_D (0.07/0.23) are approximately 1/4, as expected for the second-order method. Similarly, we could estimate that for the flat-plate wing, the solution based on the grid 86×99×114 also has approximately 1% error in the mean C_L and C_D.

Corrugated model wing A at typical values of *Re*, Φ and α

We first investigate the aerodynamic effects of corrugation of one of the above corrugated model wings (model wing A) at typical values of *Re*, Φ and α [*Re*=200, Φ=150 deg, α_d (and α_u)=40 deg]. We will consider the cases of other corrugation patterns and the corrugation effects at other values of *Re*, Φ and α below.

Fig. 6 gives the time courses of C_L, C_D and C_M, of the corrugated wing in one cycle; results for the flat-plate wing are included for comparison. The time courses of C_L, C_D and C_M of the corrugated wing are almost the same as their counterparts for the flat-plate wing, although the lift of the corrugated wing is slightly smaller than that of the flat-plate wing and the drag of the corrugated wing is slightly larger in some parts of the wingbeat cycle and slightly smaller in other parts of the wingbeat cycle than that of the flat-plate wing.

The mean lift ($\bar{C}_L$), drag ($\bar{C}_D$) and moment ($\bar{C}_M$) coefficients (averaged over the wingbeat cycle) of the corrugated wing are 1.89, 2.01 and 0.40, respectively. Their counterparts for the flat-plate wing are 1.97, 2.01 and 0.39, respectively. From the pitching moment, the chordwise location of the center of pressure can be computed (the contribution of the surface viscous stress to the pitching moment is negligible). Let *l* denote the distance between the leading edge and the center of pressure. For the corrugated wing and the flat-plate wing, the mean *l*/*c* is 0.43 and 0.42, respectively. The corrugation decreases the mean lift of the flat-plate wing by approximately 4% but has almost no effect on the mean drag and the mean location of center of pressure (the change in the mean location of center of pressure caused by the corrugation is only 0.01*c*).

Fig. 7 gives the surface pressure distributions at half-wing length at various times in the downstroke for the corrugated wing and the corresponding flat-plate wing (results in the upstroke are similar). It can be seen that in the region of the folds, the surface pressure of the corrugated wing varies around that of the flat-plate wing. That is, the corrugation only produces some local 'waves' in the surface pressure distribution, hence it has very little effect on the aerodynamic force (note that generally the surface pressure is more than one order of magnitude larger than the surface viscous stress, and the aerodynamic force on the wing is mainly due to the surface pressure).

We can use the flow information to gain some insights into the effects of wing corrugation. Fig. 8 shows the contour plots of the

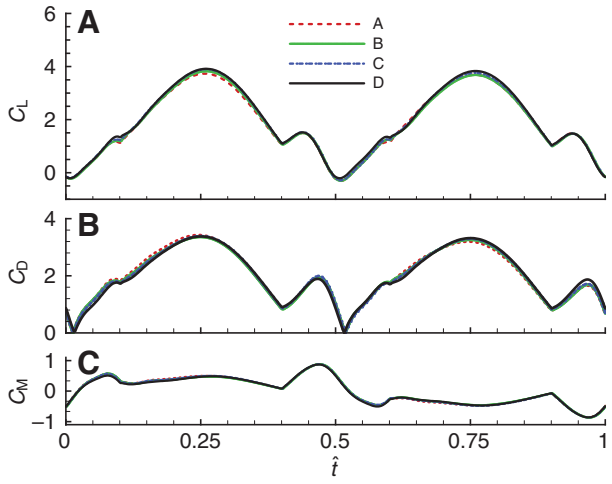

Fig. 10. Time courses of the lift (C_L), drag (C_D) and pitching moment (C_M) coefficients of various corrugated wings and the flat-plate wing at *Re*=200, Φ=150 deg and α_d (and α_u)=40 deg. Lines A, B and C show corrugated models A, B and C, respectively and line D, the flat-plate wing. *Re*, Reynolds number; Φ, stroke amplitude; α_d and α_u, down- and upstroke angles of incidence, respectively. $\hat{t}$, non-dimensional time.

Table 1. Mean lift, drag and pitching moment coefficients of various corrugated wings and a flat-plate wing at typical values of *Re*, Φ and α [*Re*=200, Φ=150 deg and α_d (and α_u)=40 deg]

Wing model*	$\bar{C}_L$	$\bar{C}_D$	$\bar{C}_M$
A	1.89	2.01	0.40 (0.43)
B	1.91	2.00	0.39 (0.41)
C	1.95	2.01	0.40 (0.43)
D	1.97	2.01	0.39 (0.42)

*A, B and C, corrugated wings models; D, flat-plate wing. $\bar{C}_L$, $\bar{C}_D$, $\bar{C}_M$, mean lift, drag and pitching moment coefficients, respectively; *Re*, Reynolds number; Φ, stroke amplitude; α_d and α_u, down- and upstroke angles of incidence, respectively. Numbers in the parentheses are the dimensionless distance between the pressure center and leading edge.

spanwise component of vorticity at half-wing length at various times in the downstroke for the corrugated wing and the corresponding flat-plate wing (the vorticity plots in the upstroke are similar). The flows are separated and with a leading edge vortex (LEV) attaching to the upper wing surface. The positive vorticity (solid lines) shed from the trailing edge of the corrugated wing (i.e. the starting vortex or trailing vortex) is almost the same as that of the flat-plate wing (see plot at $\hat{t}$=0.125). Because the total vorticity is conserved, this indicates that the corrugated wing and the flat-plate wing have approximately the same total negative vorticity around the wing. On the basis of the relationship between the aerodynamic force and the vorticity moment (e.g. Wu, 1981), the two wings would have approximately the same aerodynamic force.

It should be noted that in Fig. 8, plots of vorticity are given only for the mid-wing section. For the flapping 3-D wing, because of the finite wing length and the variation of relative velocity along the wing span, flows will be different along the wing span. Fig. 9 shows the vorticity line plots at various wing sections at the middle downstroke ($\hat{t}$=0.25). It is apparent that for both the flat-plate wing and the corrugated wing, near the wing root (r/R=0.1; r denotes the radial distance along the wing length), the LEV is very small; and as r/R becomes larger, the LEV increases. This clearly shows the 3-D features of the flow.

A possible reason for the corrugations having only a small effect on aerodynamic forces is that the wing operates at a large angle of incidence (approximately 40 deg) and the flow is separated. The large angle of incidence dominates the corrugation in determining the flow around the wing (see analysis on results of varying angle of incidence below), and for separated flow the aerodynamic forces are much less sensitive to wing shape variation.

Various corrugated model wings at typical values of *Re*, Φ and α

Here we consider the cases of different corrugation patterns at the same typical values of *Re*, Φ and α as above [*Re*=200, Φ=150 deg, α_d (and α_u)=40 deg].

Fig. 10 gives the time courses of C_L, C_D and C_M of the corrugated wings (model wings A, B and C) in one cycle; results for the flat-plate wing are included for comparison. Similar to the case of wing A, the time courses of C_L, C_D and C_M for wings B and C are almost the same as their counterparts of the flat-plate wing. Also similar to the case of wing A, the lift of wings B and C is slightly smaller than that of the flat-plate wing and the their drag is slightly larger in some parts of the wingbeat cycle and slightly smaller in other parts than that of the flat-plate wing. The mean force and moment coefficients and the mean location of center of pressure of the corrugated and flat-plate wings are given in Table 1. For all the corrugated wings considered, the effects of corrugation on aerodynamic forces are small.

Although the effects of corrugation are small, we can still identify some differences between the different corrugated wings considered here. As seen from Fig. 10 and Table 1, the corrugation effect for wing A is a little larger than that for wing B, and the corrugation effects for wing B are a little larger than that for wing C. Wings A and B have the same number of corrugation waves, but their leading-edge shape is different: wing A has a corrugation at its leading edge and wing B does not (Fig. 1). This could account for the slightly larger corrugation effect for wing A. The leading-edge shapes of wing B and wing C are the same, but wing C has less corrugation waves than wing B (Fig. 1); this could account for the corrugation effect for wing B being slightly larger than that for wing C.

Because the aerodynamic effects of corrugation in these model wings are rather small, the differences in aerodynamic effects between them are not really important. The important point here is

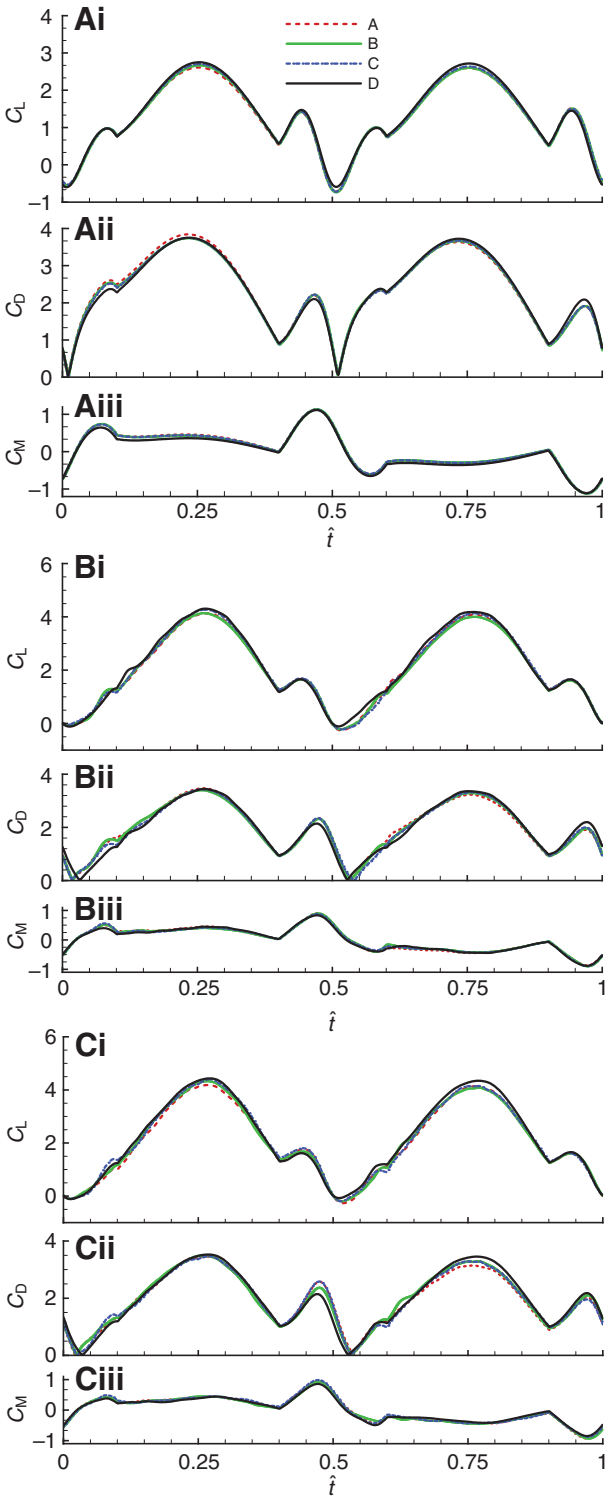

Fig. 11. Time courses of the lift (C_L), drag (C_D) and pitching moment (C_M) coefficients of the corrugated and flat-plate wings at various *Re* [Φ=150 deg, α_d (and α_u)=40 deg]. (A) *Re*=35; (B) *Re*=1800; (C) *Re*=3400. *Re*, Reynolds number; Φ, stroke amplitude; α_d and α_u, down- and upstroke angles of incidence, respectively. Lines A, B and C show corrugated models A, B and C, respectively and line D, the flat-plate wing. $\hat{t}$, non-dimensional time.

that all different corrugation patterns considered here have a very small effect on the aerodynamic forces and moments of the flapping wing.

The effects of wing corrugation at various *Re*

Computations for *Re* lower and higher than that used above were conducted (*Re*=35, 1800 and 3400). As mentioned above, in the present study the reference velocity used for *Re* was the mean flapping velocity at the radius of the second moment of wing area (r_2), thus *Re*=35 would be representative of very small insects, such as *Encarsia formosa* and *Re*=3400 would be representative of relatively large insects, such as hawkmoths and dragonflies.

Fig. 11A–C gives the time courses of C_L, C_D and C_M of the corrugated wings in one cycle at *Re*=35, 1800 and 3400, respectively; corresponding results for the flat-plate wing are included for comparison. It is seen that, similar to the case of *Re*=200, the time courses of C_L, C_D and C_M of the corrugated wings are almost the same as their counterparts of the flat-plate wing, however, when *Re* is higher (e.g. at *Re*=3400; Fig. 11C) the effects of wing corrugation are slightly larger.

The mean force and moment coefficients and the mean location of center of pressure are listed in Table 2; those for *Re*=200 are also included for comparison. It is seen that even at *Re*=3400, the magnitudes of change in the mean lift and mean drag caused by the corrugation are no more than 5 and 2% of those of the flat-plate wing, respectively. The average of the magnitudes of change in $\bar{C}_L$ and $\bar{C}_D$ resulting from the corrugation is less than 3.5%. The change in the mean location of center of pressure caused by the corrugation is no more than 0.01*c*.

Fig. 12 shows the contour plots of the spanwise component of vorticity at half-wing length at various times in the downstroke for a corrugated wing (model wing A) and the flat-plate wing at *Re*=35, and Fig. 13 shows the vorticity plots at *Re*=3400. Similar to the case of *Re*=200, the positive vorticity (solid lines) shed from the trailing edge of the corrugated wing (the starting vortex or trailing vortex) is almost the same as that of the flat-plate wing (see plots at $\hat{t}$=0, $\hat{t}$=0.125 and $\hat{t}$=0.5 in Figs 12 and 13) and the flow patterns of the corrugated wing and the flat-plate wing are approximately the same. Again, a possible reason for the small effect of corrugation on aerodynamic forces is that the wing operates at a large angle of incidence and the flow is separated: the large angle of incidence dominates the corrugation in determining the flow around the wing, and for separated flow, the aerodynamic forces are less sensitive to wing shape variation.

The effects of wing corrugation at various Φ

To see if the effects of wing corrugation would vary when the stroke amplitude is changed, three more stroke amplitudes were examined,

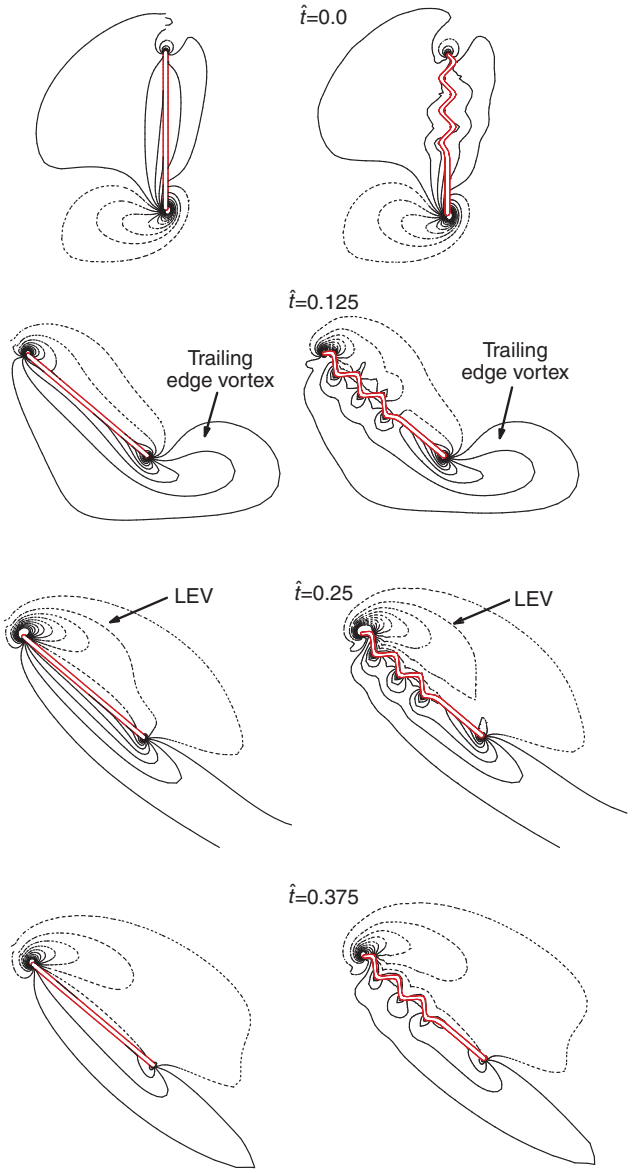

Fig. 12. Vorticity plots at half-wing length of the flat-plate wing and corrugated model wing A at various times during a downstroke at *Re*=35 [Φ=150 deg, α_d (and α_u)=40 deg]. *Re*, Reynolds number; Φ, stroke amplitude; α_d and α_u, down- and upstroke angles of incidence, respectively. Solid and broken lines indicate positive and negative vorticity, respectively. The magnitude of the non-dimensional vorticity at the outer contour is 1 and the contour interval is 3. $\hat{t}$, non-dimensional time; LEV, leading edge vortex.

Table 2. Mean lift, drag and pitching moment coefficients of the corrugated wings and a flat-plate wing at various *Re* [Φ=150 deg and α_d (and α_u)=40 deg]

	Re=35			*Re*=200			*Re*=1800			*Re*=3400		
Wing model*	$\bar{C}_L$	$\bar{C}_D$	$\bar{C}_M$	$\bar{C}_L$	$\bar{C}_D$	$\bar{C}_M$	$\bar{C}_L$	$\bar{C}_D$	$\bar{C}_M$	$\bar{C}_L$	$\bar{C}_D$	$\bar{C}_M$
A	1.30	2.38	0.42 (0.42)	1.89	2.01	0.40 (0.43)	2.08	1.98	0.37 (0.42)	2.09	1.95	0.37 (0.42)
B	1.32	2.36	0.41 (0.42)	1.91	2.00	0.39 (0.41)	2.07	1.97	0.35 (0.41)	2.12	1.98	0.36 (0.42)
C	1.33	2.36	0.41 (0.42)	1.95	2.01	0.40 (0.43)	2.12	1.96	0.36 (0.41)	2.16	1.97	0.38 (0.42)
D	1.36	2.37	0.40 (0.41)	1.97	2.01	0.39 (0.42)	2.16	1.97	0.35 (0.41)	2.21	1.99	0.34 (0.41)

*A, B and C, corrugated wings models; D, flat-plate wing. $\bar{C}_L$, $\bar{C}_D$, $\bar{C}_M$, mean lift, drag and pitching moment coefficients, respectively; *Re*, Reynolds number; Φ, stroke amplitude; α_d and α_u, down- and upstroke angles of incidence, respectively. Numbers in the parentheses are the dimensionless distance between pressure center and leading edge.

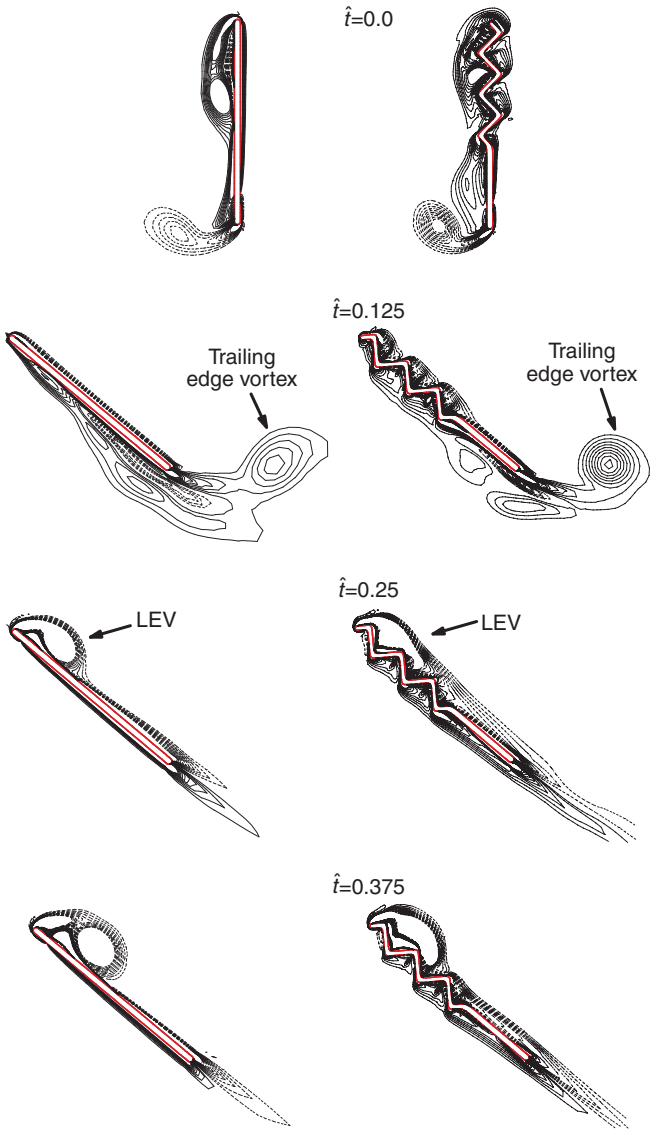

Fig. 13. Vorticity plots at half-wing length of the flat-plate wing and corrugated model wing A at various times during a downstroke at *Re*=3400 [Φ=150 deg, α_d (and α_u)=40 deg]. *Re*, Reynolds number; Φ, stroke amplitude; α_d and α_u, down- and upstroke angles of incidence, respectively. Solid and broken lines indicate positive and negative vorticity, respectively. The magnitude of the non-dimensional vorticity at the outer contour is 4 and the contour interval is 3. $\hat{t}$, non-dimensional time; LEV, leading edge vortex.

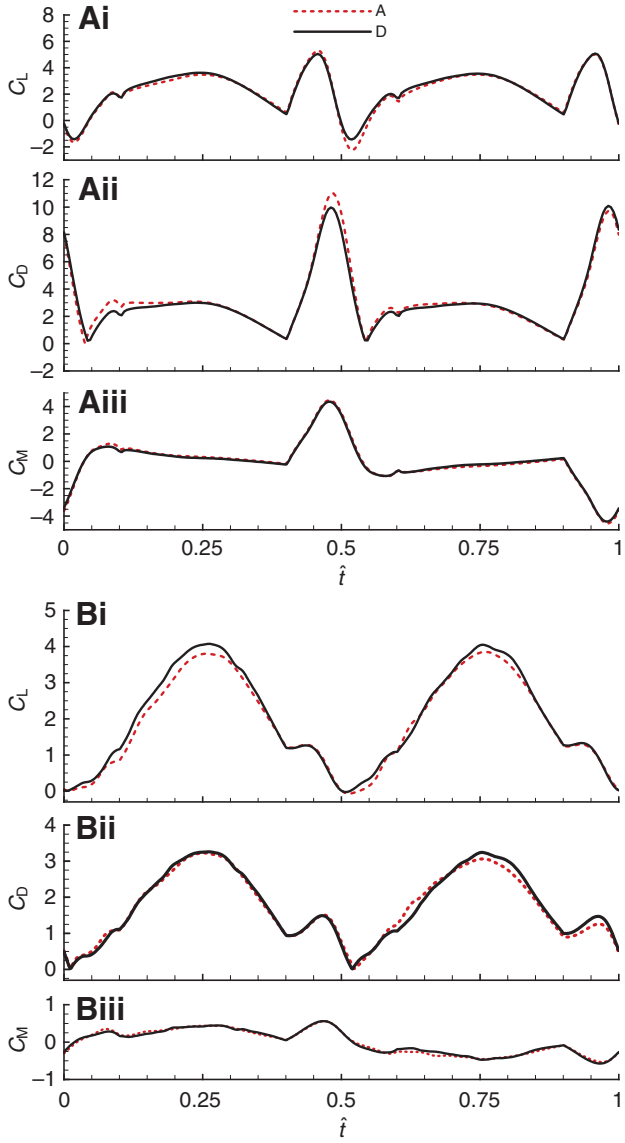

Fig. 14. Time courses of the lift (C_L), drag (C_D) and pitching moment (C_M) coefficients of corrugated model wing A (A lines) and the flat-plate wing (D lines) at various stroke amplitudes (Φ) [*Re*=1800, α_d (and α_u)=40 deg]. (A) Φ=70 deg; (B) Φ=180 deg. *Re*, Reynolds number; α_d and α_u, down- and upstroke angles of incidence, respectively. $\hat{t}$, non-dimensional time.

Φ=180, 110 and 70 deg (one larger and two smaller than the Φ value considered above), were investigated for a corrugated wing (model wing A) and the flat-plate wing [at *Re*=1800 and α_d (and α_u)=40 deg]. Φ=180 deg is about the largest stroke amplitude an insect can use because of its geometrical restriction; Φ=70 deg is about the smallest stroke amplitude insects use [hoverflies hovering with an inclined stroke plane and some dragonflies use such a small Φ (see Ellington, 1984; Dudley, 2000)].

Fig. 14A,B gives the time courses of C_L, C_D and C_M of the corrugated wing in one cycle at Φ=70 and 180 deg, respectively, compared with the corresponding results of the flat-plate wing. Similar to the case of Φ=150, the time courses of C_L, C_D and C_M of the corrugated wings are almost the same as those of the flat-plate wing. The mean force and moment coefficients and the mean location of center of pressure are listed in Table 3. The magnitude of change in the mean lift caused by the corrugation is approximately 4% of that of the flat-plate wing at all the Φ values; the magnitude of change in the mean drag caused by the corrugation is approximately 1% at Φ=180 deg and increases to approximately 4% at Φ=70 deg. The average of the magnitudes of change in the mean lift and mean drag due to the corrugation is 2.5% at Φ=180 deg and 4% at Φ=70 deg. The change in the mean location of center of pressure caused by the corrugation is 0.01*c* at Φ=180 deg and 0.02*c* at Φ=70 deg. When the stroke amplitude changes from Φ=70 deg to 180 deg, the effect of wing corrugation varies only slightly.

Table 3. Mean lift, drag and pitching moment coefficients of corrugated wing model A and a flat-plate wing at various Φ[*Re*=1800; α_d (and α_u)=40 deg]

	Φ=70			Φ=110			Φ=150			Φ=180		
Wing model*	$\bar{C}_L$	$\bar{C}_D$	$\bar{C}_M$	$\bar{C}_L$	$\bar{C}_D$	$\bar{C}_M$	$\bar{C}_L$	$\bar{C}_D$	$\bar{C}_M$	$\bar{C}_L$	$\bar{C}_D$	$\bar{C}_M$
A	2.23	3.22	1.01 (0.43)	1.99	2.14	0.48 (0.42)	2.08	1.98	0.37 (0.42)	1.92	1.75	0.30 (0.41)
D	2.31	3.08	0.94 (0.41)	2.06	2.09	0.44 (0.42)	2.16	1.97	0.35 (0.41)	2.03	1.78	0.29 (0.40)

*A, corrugated wing model A; D, flat-plate wing. $\bar{C}_L$, $\bar{C}_D$, $\bar{C}_M$, mean lift, drag and pitching moment coefficients, respectively; *Re*, Reynolds number; Φ, stroke amplitude; α_d and α_u, down- and upstroke angles of incidence, respectively. Numbers in the parentheses are the dimensionless distance between pressure center and leading edge.

Table 4. Mean lift, drag and pitching moment coefficients of corrugated wing model A and a flat-plate wing at various angles of incidence (*Re*=1800; Φ=150 deg)

	$\bar{C}_L$		$\bar{C}_D$		$\bar{C}_M$	
α_d (and α_u; deg)	D	A	D	A	D	A
15	0.70	0.61	0.74	0.83	0.23 (0.37)	0.26 (0.41)
20	0.98	0.90	0.81	0.88	0.20 (0.37)	0.23 (0.41)
25	1.30	1.20	1.03	1.09	0.22 (0.37)	0.25 (0.39)
30	1.65	1.55	1.37	1.41	0.29 (0.38)	0.32 (0.40)
35	1.92	1.83	1.63	1.65	0.30 (0.39)	0.33 (0.41)
40	2.16	2.08	1.97	1.98	0.35 (0.41)	0.37 (0.42)
45	2.29	2.24	2.37	2.35	0.41 (0.41)	0.41 (0.41)
50	2.29	2.25	2.77	2.71	0.47 (0.40)	0.47 (0.42)
55	2.29	2.21	3.26	3.12	0.56 (0.42)	0.52 (0.41)
60	2.11	2.18	3.61	3.65	0.62 (0.42)	0.63 (0.42)

$\bar{C}_L$, $\bar{C}_D$, $\bar{C}_M$, mean lift, drag and pitching moment coefficients, respectively; *Re*, Reynolds number; Φ, stroke amplitude; α_d and α_u, down- and upstroke angles of incidence, respectively. Numbers in the parentheses are the dimensionless distance between pressure center and leading edge.

The effects of wing corrugation at various α

In above sections, the only angles of incidence of the wing considered were α_d (and α_u)=40 deg, but it is of interest to see how the effects of wing corrugation would vary when the angle of incidence is changed. Nine more angles of incidence (four larger and five smaller than 40 deg) were considered for a corrugated wing (model wing A) and the flat-plate wing [at *Re*=1800 and Φ=150 deg].

Fig. 15 shows the time courses of C_L, C_D and C_M of the corrugated and flat-plate wings in one cycle at a relatively small angle of incidence [α_d (and α_u)=20 deg]. Comparing the results in Fig. 15 with that at a relatively large angle of incidence [Fig. 11B; α_d (and α_u)=40 deg], it can be seen that the effects of wing corrugation become larger at smaller angle of incidence. The mean force and moment coefficients and mean location of center of pressure for all

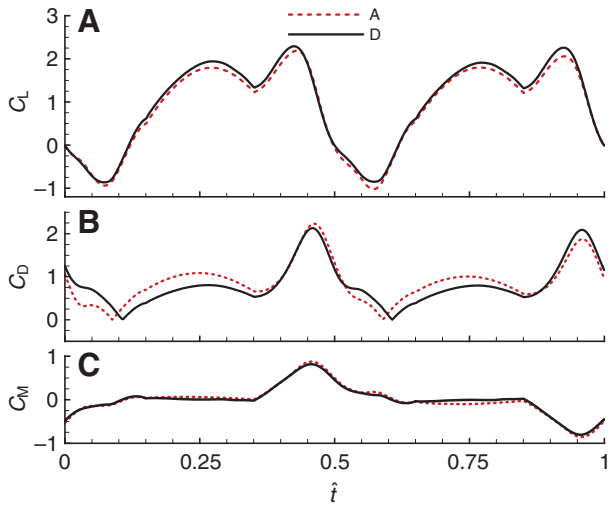

Fig. 15. Time courses of the lift (C_L), drag (C_D) and pitching moment (C_M) coefficients of corrugated model wing A (A lines) and the flat-plate wing (D lines) at α_d (and α_u)=20 deg (*Re*=1800, Φ=150 deg). *Re*, Reynolds number; Φ, stroke amplitude; α_d and α_u, down- and upstroke angles of incidence, respectively. $\hat{t}$, non-dimensional time.

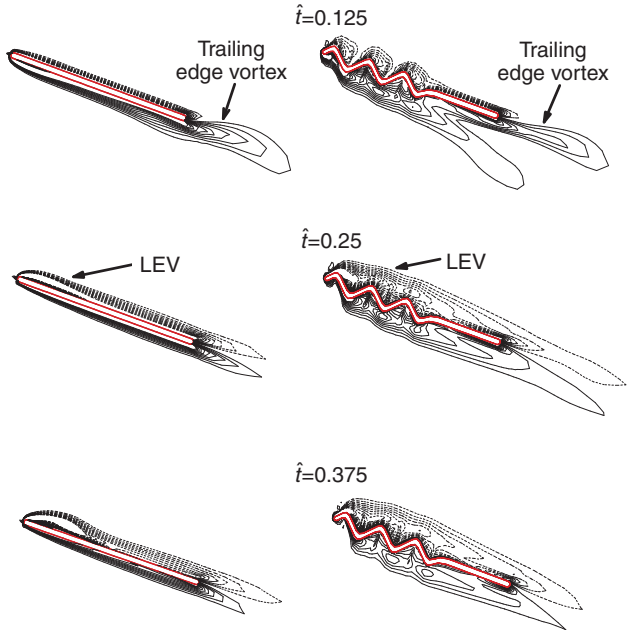

Fig. 16. Vorticity plots at half-wing length of the flat-plate wing and corrugated model wing A at various times during a downstroke at α_d (and α_u)=20 deg (*Re*=1800, Φ=150 deg). *Re*, Reynolds number; Φ, stroke amplitude; α_d and α_u, down- and upstroke angles of incidence, respectively. $\hat{t}$, non-dimensional time; LEV, leading edge vortex.

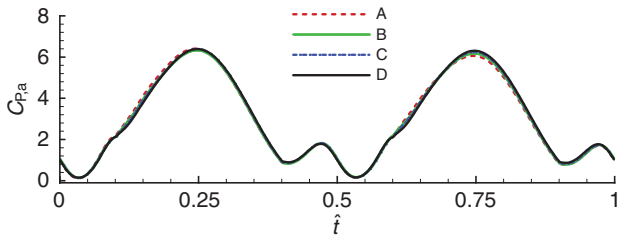

Fig. 17. Time courses of the aerodynamic power coefficient ($C_{P,a}$) of various corrugated wings and the flat-plate wing at *Re*=200, Φ=150 deg and α_d (and α_u)=40 deg. Lines A, B and C show corrugated model wings A, B and C, respectively; line D shows the flat-plate wing. *Re*, Reynolds number; Φ, stroke amplitude; α_d and α_u, down- and upstroke angles of incidence, respectively. $\hat{t}$, non-dimensional time.

angles of incidence considered are given in Table 4. When the angle of incidence is above 35 deg, the magnitudes of change in the mean lift and mean drag caused by the corrugation are less than 5% of those of the flat-plate wing and the change in the mean location of center of pressure caused by the corrugation is less than 0.02*c*, whereas when the angle of incidence is small, e.g. below 20 deg, the magnitudes of change in the mean lift and mean drag become relatively large, approximately 10–15% of those of the flat-plate wing, and the change in the mean location of center of pressure is also relatively large, approximately 0.04*c* (but it should be noted that insects when hovering and flying at low speed usually do not use such small angles of incidence) (see Ellington, 1984; Ennos, 1989; Walker et al., 2009).

As observed above, at relatively large angle of incidence [α_d (and α_u)=40 deg], the flow patterns of the corrugated wing and the flat-plate wing are approximately the same [see Figs 8 and 9]. Here, we examine the flow patterns of the corrugated wing and the flat-plate wing at a relatively small angle of incidence [α_d (and α_u)=20 deg]. Fig. 16 shows the contour plots of the spanwise component of vorticity at half-wing length. Comparing the flow patterns in Fig. 16 with those in Fig. 8, it is apparent that, at a small angle of incidence, differences between the flow patterns of the corrugated and the flat-plate wings are relatively large. This clearly shows that when it is large, the angle of incidence dominates the corrugation in determining the flow around the wing, but when it gets smaller, the wing corrugation can affect the flow more.

Table 5. Mean aerodynamic power coefficient of the corrugated wings and a flat-plate wing at various *Re* [Φ=150 deg and α_d (and α_u)=40 deg]

	$\bar{C}_{P,a}$			
Wing model*	*Re*=35	*Re*=200	*Re*=1800	*Re*=3400
A	3.42	2.99	2.99	2.98
B	3.39	2.98	3.00	3.03
C	3.40	3.00	2.99	3.02
D	3.43	3.00	2.99	3.05

*A, B and C, corrugated wings models; D, flat-plate wing. $\bar{C}_{P,a}$, mean aerodynamic power coefficient; *Re*, Reynolds number; Φ, stroke amplitude; α_d and α_u, down- and upstroke angles of incidence, respectively.

The effects of wing corrugation on aerodynamic power

Aerodynamic power (P_a) of the above flapping wings is determined by the following equation:

$$P_a = Q\,\dot{\phi} + M\,\dot{\alpha}\,, \quad (5)$$

where Q is the torque about the axis perpendicular to the stroke plane (which is produced by the drag), M is the pitching moment, and $\dot{\alpha}$ is the rotation speed.

During the stroke reversal phases, $\dot{\phi}$ is close to zero, $\dot{\alpha}$ is large (see Fig. 2B) and the aerodynamic power is mainly due to the pitching moment M (see Eqn 5). In the above sections, it was shown that the corrugation only just affects the pitching moment. Hence the corrugation would have little effect on aerodynamic power during the stroke reversal phases.

During the translation phases, $\dot{\alpha}$ is zero and $\dot{\phi}$ is large (see Fig. 2B), the aerodynamic power comes from the torque of the drag Q (see Eqn 5). Q is dependent on the drag and the spanwise location of the line of action of the drag. In the above sections, we discussed the effects of corrugation on the drag and showed that the corrugation has very small effects on the drag. However, we do not know if the corrugation affects the spanwise location of the line of action of the drag, hence do not know how the corrugation affects the aerodynamic power in the translation phases.

Here we compute aerodynamic power coefficients of the wings and investigate how the corrugation affects the aerodynamic power. Fig. 17 gives the time courses of the aerodynamic power coefficient (denoted by $C_{P,a}$, defined as P_a non-dimensionalized by $0.5\rho U^3 Sc$) of the corrugated wings and the flat-plate wing in one cycle, at *Re*=200, Φ=150 deg, α_d (and α_u)=40 deg (results at other *Re*, Φ, α_d and α_u were similar). During the stroke reversal phases ($\hat{t}$=0–0.1, $\hat{t}$=0.4–0.6 and $\hat{t}$=0.9–1), the corrugation has little effect on aerodynamic power. This is expected because the corrugation only just affects the pitching moment. During the translation phases ($\hat{t}$=0.1–0.4 and $\hat{t}$=0.6–0.9), the corrugation has a slight effect on the aerodynamic power. Comparing the aerodynamic power in the translation phases in Fig. 17 ($\hat{t}$=0.1–0.4 and $\hat{t}$=0.6–0.9) with those for the drag in Fig. 10, we find that the effect of corrugation on the aerodynamic power is almost the same as that on the drag. This shows that the corrugation has little effect on the spanwise location of the line of action of the drag. The mean $C_{P,a}$ ($\bar{C}_{P,a}$) is given in Table 5. Wing corrugation only has a small effect on the mean aerodynamic power coefficient, similar to drag.

Table 6. Mean lift, drag and pitching moment coefficients of corrugated wing model A and a flat-plate wing at various aspect ratios [*Re*=1800; α_d (and α_u)=40 deg]

	Aspect ratio 6			Aspect ratio 7			Aspect ratio 8			Aspect ratio 9		
Wing model*	$\bar{C}_L$	$\bar{C}_D$	$\bar{C}_M$	$\bar{C}_L$	$\bar{C}_D$	$\bar{C}_M$	$\bar{C}_L$	$\bar{C}_D$	$\bar{C}_M$	$\bar{C}_L$	$\bar{C}_D$	$\bar{C}_M$
A	2.08	1.98	0.37 (0.42)	2.06	1.88	0.36 (0.41)	2.01	1.79	0.35 (0.41)	2.03	1.77	0.34 (0.41)
D	2.16	1.97	0.35 (0.41)	2.11	1.86	0.35 (0.41)	2.08	1.81	0.35 (0.41)	2.06	1.80	0.35 (0.41)

$\bar{C}_L$, $\bar{C}_D$, $\bar{C}_M$, mean lift, drag and pitching moment coefficients, respectively; *Re*, Reynolds number; Φ, stroke amplitude; α_d and α_u, down- and upstroke angles of incidence, respectively. Numbers in the parentheses are the dimensionless distance between pressure center and leading edge.

Results at various wing aspect ratios

In the above sections, wings with an R/c ratio of 3 (aspect ratio of 6) were considered. R/c ratios of insects range from approximately 2.5 to 5 [aspect ratio from 5 to 10 (see Dudley, 2000). Next we examined whether the effects of wing corrugation would vary when the R/c ratio was increased. Three more R/c ratios, 3.5, 4 and 4.5 (aspect ratios, 7, 8 and 9), were considered for corrugated model wing A and the flat-plate wing [at Re=1800 and Φ=150 deg]. For the corrugated wing, when the R/c ratio was 3, as described above, the number of spanwise grid points was 70; when the R/c ratio is increased to 3.5, 4 and 4.5, the number of spanwise grid points is increased to 84, 99 and 114, respectively, to keep the grid density unchanged when the wing length is increased. These spanwise grid points, 84, 99 and 114, were also used for the corresponding flat-plate wings of R/c ratios of 3.5, 4 and 4.5, respectively.

Fig. 18A–C show the time courses of C_L, C_D and C_M of the corrugated and flat-plate wings of R/c ratios 3.5, 4 and 4.5 (aspect ratios 7, 8 and 9), respectively, in one cycle. Table 6 gives the mean force and moment coefficients ($\bar{C}_L$, $\bar{C}_D$ and $\bar{C}_M$) and the mean location of center of pressure [for comparison, the results for R/c ratio 3 (aspect ratio 6) are also included].

It is seen that for the wings with larger aspect ratios, similar to the case of the wing with an aspect ratio of 6, the magnitude of change in the mean lift or the mean drag caused by the corrugation is no more than 4% of that of the flat-plate wing, and the change in the mean location of center of pressure caused by the corrugation is no more than 0.01c. These results show that change in aspect ratio has little influence on the effect of corrugation.

Change in aspect ratio has little influence on the aerodynamic force and moment coefficients of the flapping wings. For example, for the flat-plate wings, when the aspect ratio changes from 6 to 9, $\bar{C}_L$ changes from 2.16 to 2.06, $\bar{C}_D$ changes from 1.97 to 1.80 and $\bar{C}_M$ is almost unchanged. This is in agreement with the experimental data of Usherwood and Ellington and the computational data of Luo and Sun [Usherwood and Ellington measured the aerodynamic forces of revolving wings and Luo and Sun computed the aerodynamic forces of wings performing a sweeping motion; both studies showed that change in aspect ratio had only a very small influence on the aerodynamic force and moment coefficients of the wings (Usherwood and Ellington, 2002a; Usherwood and Ellington, 2002b; Luo and Sun, 2005).]

Some discussions on modeling the wing as a flat plate

In the study of the aerodynamics of insect flapping wings using experimental and computational models, if wing corrugation needs to be modeled, the experimental wing model would be much more difficult to manufacture and the computational wing model would need quite complex and dense grids. Furthermore, it is difficult to measure the exact corrugation of the wing of an insect in free-flight conditions. Therefore, it is of great interest to know how well a rigid flat-plate wing can model the corrugated wing.

The above results show that at typical angles of incidence of hovering insects wings [35–50 deg (see Ellington, 1984; Ennos, 1989; Walker et al., 2009)], the time courses of the force and moment coefficients (C_L, C_D and C_M) of the corrugated wing are very similar to those of the rigid flat-plate wing, and the magnitude of change in the mean aerodynamic forces caused by the corrugation is less than 5% of that of the flat-plate wing and the location of center of pressure and the aerodynamic power required are little affected by the corrugation. Thus, using a flat-plate wing to model the corrugated wing is a good approximation.

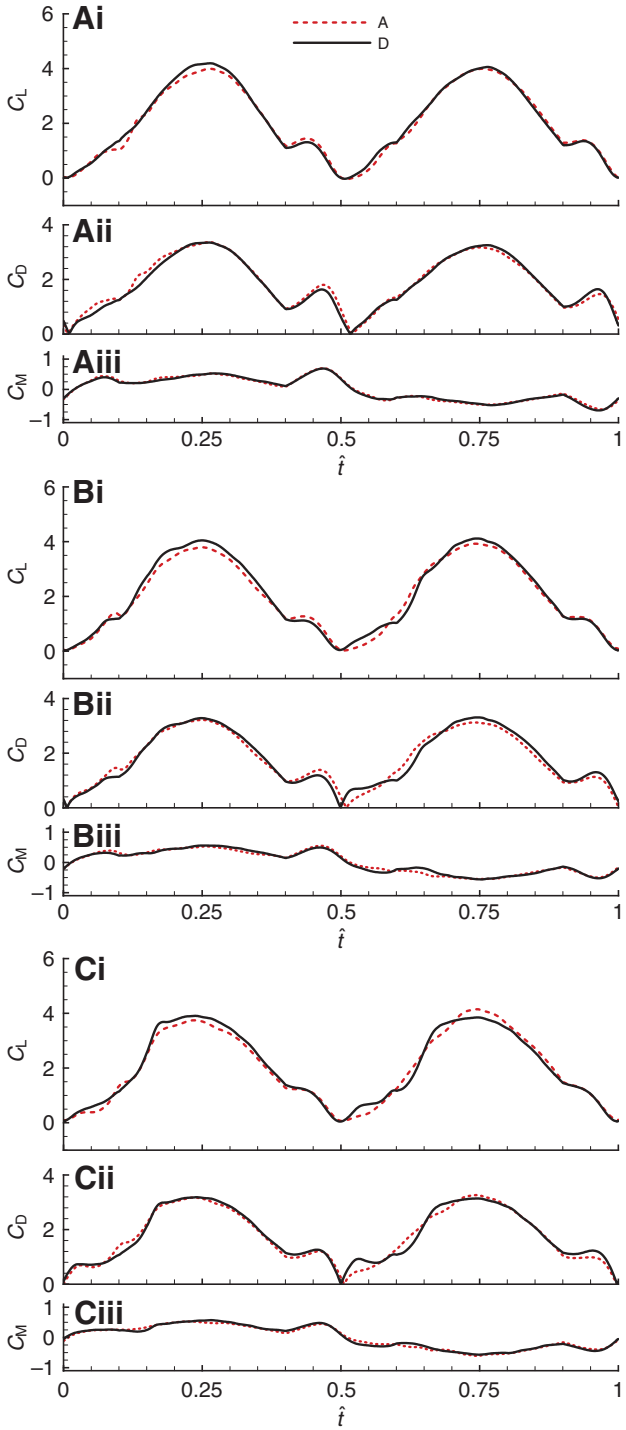

Fig. 18. Time courses of the lift (C_L), drag (C_D) and pitching moment (C_M) coefficients of corrugated model wing A and the flat-plate wing of various R-to-c or aspect ratios [Re=1800, α_d (and α_u)=40 deg]. A, B and C show aspect ratios=7, 8 and 9, respectively. Re, Reynolds number; Φ, stroke amplitude; α_d and α_u, down- and upstroke angles of incidence, respectively. $\hat{t}$, non-dimensional time.

The above results show that the corrugation does not have obvious aerodynamic advantages or shortcomings. But its structural advantages are well known. To provide aerodynamic forces effectively and efficiently, an insect wing needs to be light for fast flapping motion and at the same time to be stiff enough to maintain certain aerodynamic shape. Researchers have shown that corrugation

plays an essential role in meeting these requirements; for example, Rees, using a theoretical model, calculated that the use of corrugation greatly increased both the stiffness and strength of insect wings (Rees, 1975b), Newman and Wootton showed that in such corrugations, the membrane of the wing could stiffen the wing by means of a 'stress skin' effect (Newman and Wootton, 1986), and Ennos, by means of theoretical modeling and experimental measurement, further showed that the corrugation of an insect wing gave desirable wing deformation (camber and twist) during flapping flight (Ennos, 1988). We thus see that the corrugation provides structural advantages without producing negative aerodynamic effect.

LIST OF SYMBOLS AND ABBREVIATIONS

c	chord length
C_D	drag coefficient
CFD	computational fluid dynamics (CFD)
C_L	lift coefficient
$C_{P,a}$	aerodynamic power coefficient
D	drag
L	lift
LEV	leading edge vortex
M	pitching moment
MAV	micro-aerial vehicles
n	wingbeat frequency
P_a	aerodynamic power
Q	torque about the axis perpendicular to the stroke plane
R	wing length
Re	Reynolds numbers
S	wing area
t	time
$\hat{t}$	non-dimensional time parameter
$\mathbf{u}$	fluid velocity field
U	mean flapping velocity
∇	gradient operator
∇^2	Laplacian operator
α_d	mid downstroke angle of incidence
α_u	mid upstroke angle of incidence
$\dot{\alpha}$	rotation speed
Δt_r	time interval of wing rotation during the stroke reversal
Δt_r^*	non-dimensional time interval of wing rotation
ρ	fluid density
ϕ	positional angle
$\dot{\phi}$	wing translation speed
Φ	stroke amplitude

ACKNOWLEDGEMENTS

This research was supported by grants from the National Natural Science Foundation of China (10732030) and the 111 Project (B07009).

REFERENCES

Dickinson, M. H., Lehman, F. O. and Sane, S. P. (1999). Wing rotation and the aerodynamic basis of insect flight. *Science* **284**, 1954-1960.
Du, G. and Sun, M. (2010). Effects of wing deformation on aerodynamic forces in hovering hoverflies. *J. Exp. Biol.* **213**, 2273-2283.
Dudley, R. (2000). *The Biomechanics of Insect Flight: Form, Function, Evolution.* Princeton, NJ: Princeton University Press.
Ellington, C. P. (1984). The aerodynamics of hovering insect flight. III. Kinematics. *Philos. Trans. R. Soc. Lond. B* **305**, 41-78.
Ellington, C. P., Van Den Berg, C., Willmott, A. P. and Thomas, A. L. R. (1996). Leading-edge vortices in insect flight. *Nature* **384**, 626-630.
Ennos, A. R. (1988). The importance of torsion in the design of insect wings. *J. Exp. Biol.* **140**, 137-160.
Ennos, A. R. (1989). The kinematics and aerodynamics of the free flight of some Diptera. *J. Exp. Biol.* **142**, 49-85.
Hilgenstock, A. (1988). A fast method for the elliptic generation of three dimensional grids with full boundary control. *Numerical Grid Generation In CFM'88* (ed. S. Sengupta, J. Hauser, P. R. Eiseman and J. F. Thompson), pp.137-146. Swansea, UK: Pineridge Press Ltd.
Kesel, A. B. (2000). Aerodynamic characteristics of dragonfly wing sections compared with technical aerofoils. *J. Exp. Biol.* **203**, 3125-3135.
Liu, H., Ellington, C. P., Kawachi, K., Van Den Berg, C. and Willmott, A. P. (1998). A computational fluid dynamic study of hawkmoth hovering. *J. Exp. Biol.* **201**, 461-477.
Liu, Y. and Sun, M. (2008). Wing kinematics measurement and aerodynamics of hovering droneflies. *J. Exp. Biol.* **211**, 2014-2025.
Luo, G. and Sun, M. (2005). The effects of corrugation and wing planform on the aerodynamic force production of sweeping model insect wings. *Acta Mech. Sinica* **21**, 531-541.
Newman, D. J. S. and Wootton, R. J. (1986). An approach to the mechanics of pleating in dragonfly wings. *J. Exp. Biol.* **125**, 361-372.
Rees, C. J. C. (1975a). Aerodynamic properties of an insect wing section and a smooth aerofoil compared. *Nature* **258**, 141-142.
Rees, C. J. C. (1975b). Form and function in corrugated insect wings. *Nature* **256**, 200-203.
Rogers, S. E. and Kwak, D. (1990). Upwind differencing scheme for the time-accurate incompressible Navier-Stokes equations. *AIAA J.* **28**, 253-262.
Rogers, S. E., Kwak, D. and Kiris, C. (1991). Steady and unsteady solutions of the incompressible Navier-Stokes equations. *AIAA J.* **29**, 603-610.
Sane, S. P. and Dickinson, M. H. (2001). The control of flight force by a flapping wing: lift and drag production. *J. Exp. Biol.* **204**, 2607-2626.
Sun, M. and Tang, J. (2002). Unsteady aerodynamic force generation by a model fruit fly wing in flapping motion. *J. Exp. Biol.* **205**, 55-70.
Sun, M. and Wu, J. H. (2003). Aerodynamic force generation and power requirements in forward flight in a fruit fly with modeled wing motion. *J. Exp. Biol.* **206**, 3065-3083.
Sun. M. and Yu, X. (2006). Aerodynamic force generation in hovering flight in a tiny insect. *AIAA J.* **44**, 1532-1540.
Usherwood, J. R. and Ellington, C. P. (2002a). The aerodynamics of revolving wings. I. Model hawkmoth wings. *J. Exp. Biol.* **205**, 1547-1564.
Usherwood, J. R. and Ellington, C. P. (2002b). The aerodynamics of revolving wings. II. Propeller force coefficients from mayfly to quail. *J. Exp. Biol.* **205**, 1565-1576.
Vargas, A., Mittal, R. and Dong, H. (2008). A computational study of the aerodynamic performance of a dragonfly wing section in gliding flight. *Bioinspiration and Biomimetics* **3**, 026004.
Wang, Z. J., Birch, J. M. and Dickinson, M. H. (2004). Unsteady forces and flows in flow Reynolds number hovering flight: two-dimensional computational *vs* robotic wing experiments. *J. Exp. Biol.* **207**, 269-283.
Walker, S. M., Thomas, A. L. R. and Taylor, G. K. (2009). Deformable wing kinematics in free-flying hoverflies. *J. R. Soc. Interface* **7**, 131-142.
Wu, J. C. (1981). Theory for aerodynamic force and moment in viscous flows. *AIAA J.* **19**, 432-441.
Wu, J. H. and Sun, M. (2004). Unsteady aerodynamic forces of a flapping wing. *J. Exp. Biol.* **207**, 1137-1150.